

## Article

# Utilizing Dynamic Scattering for Learning Radar Cross-Section of a Flapping-Wing Aircraft

Zeyang Zhou \*  and Jun Huang

School of Aeronautic Science and Engineering, Beihang University, Beijing 100191, China

\* Correspondence: zeyangzhou@buaa.edu.cn

**Abstract:** To study the radar cross-section (RCS) of a flapping-wing aircraft, a method of flapping-wing dynamic scattering is presented. The aircraft has two rigid wings and a fuselage similar to a bird's body, where the plane shape of the wing is U-type. The aircraft model is established and the pitching and flapping actions of the wing are simulated. The electromagnetic scattering characteristics of aircraft under two flight modes, different radar wave frequencies and observation angles are investigated. The results show that in the given gliding mode, the fuselage provides the main contribution to the lateral peak value. For the given forward azimuth range in the flapping mode, increasing the azimuth can reduce the mean and peak of the aircraft dynamic RCS curve, while increasing the elevation angle will increase the peak and mean of the aircraft dynamic RCS curve. In the flapping mode, the mean RCS of the aircraft in the lateral backward azimuth is significantly lower than that in the lateral forward azimuth. For the given tail azimuth range, the increase of azimuth will increase the mean and peak level of aircraft dynamic RCS curve. The presented method is effective to study the dynamic RCS characteristics of the flapping-wing aircraft.

**Keywords:** flapping wing; radar cross-section; dynamic electromagnetic scattering; radar stealth; bionic aircraft



**Citation:** Zhou, Z.; Huang, J. Utilizing Dynamic Scattering for Learning Radar Cross-Section of a Flapping-Wing Aircraft. *Photonics* **2022**, *9*, 877. <https://doi.org/10.3390/photonics9110877>

Received: 27 September 2022

Accepted: 16 November 2022

Published: 19 November 2022

**Publisher's Note:** MDPI stays neutral with regard to jurisdictional claims in published maps and institutional affiliations.



**Copyright:** © 2022 by the authors. Licensee MDPI, Basel, Switzerland. This article is an open access article distributed under the terms and conditions of the Creative Commons Attribution (CC BY) license (<https://creativecommons.org/licenses/by/4.0/>).

## 1. Introduction

Imitating birds in nature in shape, structure and flight principle, flapping wing aircraft can better hide or not be easily found when flying in the air. With thin wings and small fuselage, the overall level of radar cross-section (RCS) of flapping wing aircraft is low [1–3], while the change of RCS caused by wing flapping up and down has become a difficulty in the research of stealth performance of flapping wing aircraft.

The ideas used in the development of flapping wing aircraft include morphological bionics, structural bionics and functional bionics. Considering the dynamic similarity with insects on earth, flapping wing robots fly on Mars through bionic dynamics [4]. Based on the aerodynamic calculation method of flexible large deformation flapping wing, experiments under different flapping frequency, angle of attack and velocity are carried out in a low-speed wind tunnel [5]. The flapping wing aircraft has an X-shaped flapping wing configuration, a tail control surface for roll and pitch control, and a tail rotor for yaw control [6]. The plane shape of the wing of the flapping wing machine adopts a 1/4 elliptical contour, and the small motor installed on the fuselage forces the wings to flutter up and down [7]. Flapping wing unmanned aerial vehicle can fly silently at a low speed, and its application has become the focus of attention [8–10]. Flapping wing aircraft has the advantages of integrating lifting, hovering and propulsion functions [11], thus it can fly long distances with very little energy, while it has strong mobility and flexibility, and is more suitable for reconnaissance missions.

The scattering sources of flapping wing aircraft mainly come from the aircraft body and flapping wings. The geometric model of the blade is established, and the physical optics (PO) and the equivalent current method are used to calculate the RCS data, where

the quasi-static principle (QSP) is used to simulate various movements of the target [12–14]. A complex target is divided into several triangular or quadrilateral surface elements to approximate the electromagnetic calculation model [15]. Remove a portion of the metal from the radiator and implement a periodic slot adjacent to the radiation edge. These slots reduce the vertical reflection of the radiator, which results in a reduction in the single station RCS [16]. The grid adjoint equation at each time step level is established, and then the adjoint variables of all time steps in a cycle are solved by time inverse integration [17]. The design of a low RCS millimeter-wave antenna array is presented to reduce the reflections toward the car fascia [18]. Control the timing of wing merging and separation to realize that the wing can complete two down pours and one up pours in one cycle [19]. Using the finite-element domain decomposition method, the statistical characteristics of bistatic RCS under horizontal and vertical polarization are obtained [20]. The multi-stage modeling method is adopted, and the wing is divided into inner wing and outer wing [21]. It can be seen that there are a wide range of factors affecting the RCS of flapping wing aircraft [22–24], such as flexible or rigid wing, observation angle [25–27], body configuration, radar wave frequency [28–30], polarization mode, wing pitch and flapping [31], and flight state. The body of the tilt rotor aircraft has adopted a preliminary stealth design, and the dynamic RCS of the rotor and the whole aircraft have been investigated and discussed under given electromagnetic wave conditions [32,33]. It could be seen that the dynamic electromagnetic scattering characteristics of a wide range of targets are worth exploring, including but not limited to flapping wing aircraft, helicopters, tilt rotor aircraft and warships.

As mentioned, flapping wing aircraft has strong mobility and low-speed flight ability, which is suitable for long range cruise and reconnaissance missions, while there are few studies on the stealth performance of flapping wing. In view of the complexity of flapping wing motion, it is a challenge to deal with the electromagnetic scattering characteristics of the whole flapping wing aircraft. Therefore, this paper attempts to establish a dynamic scattering method to solve the RCS of flapping wing aircraft, where the wing is set as a rigid body model, the aircraft fuselage refers to the body shape of birds, and the flapping and pitching actions of the wing are simulated. It is of engineering value to study the dynamic RCS of flapping wing aircraft.

In this manuscript, the method is presented in Section 2. Models are built in Section 3. The results are discussed in detail in Section 4. Finally, the full text is summarized.

## 2. Flapping-Wing Scattering Method

The schematic of the dynamic electromagnetic scattering of the U-type flapping wings aircraft is shown in Figure 1, where  $A_f$  is the flapping angle of the wing,  $A_p$  represents the pitch angle of the wing, additional numerical subscripts are used to distinguish different wing numbers.  $\alpha$  is the azimuth between the radar station and the flapping wings aircraft,  $\beta$  is the elevation between the radar station and the aircraft,  $f_{rh}$  represents radar wave frequency and horizontal polarization. Note that the wing model similar to the plane geometry of bird wings can refer to Figure A1 in Appendix A, and the relevant results can refer to Figures A1 and A2.

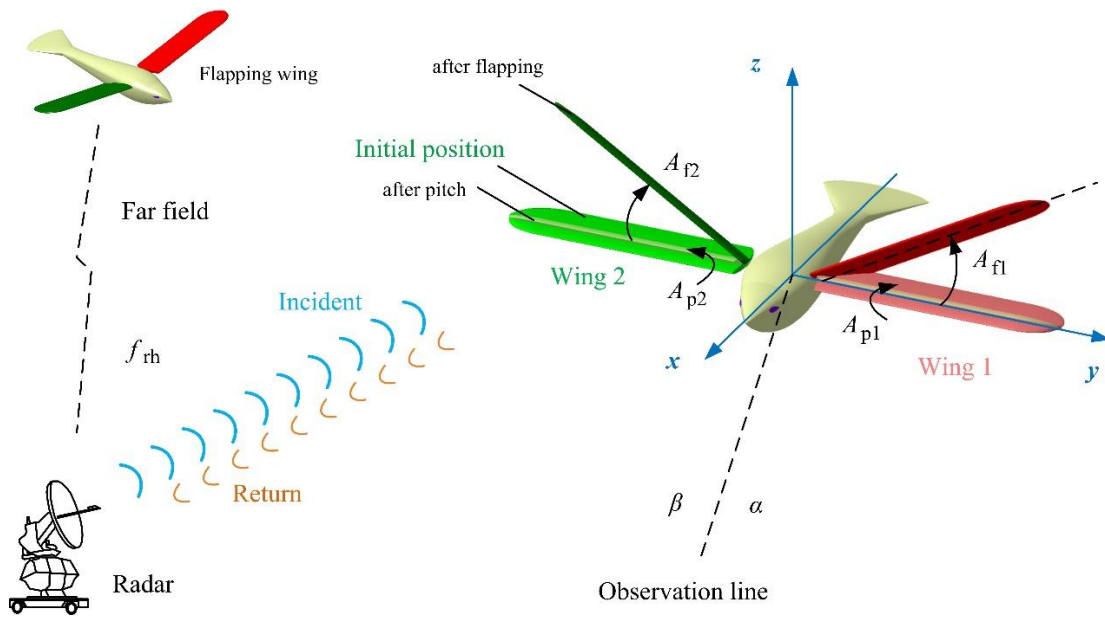


**Figure 1.** Schematic of the dynamic electromagnetic scattering of the flapping-wing aircraft.

2.1. Flapping-Wing Motion

When the aircraft is flapping, the flapping angle is controlled in the following manner:

$$A_{f1}(t) = A_{k1} \sin(\omega_{k1}t + B_{k1}) + C_{k1}, \quad t \in [ 0, T_{flap}/2 ) \tag{1}$$

where  $t$  is time. The current flapping mode is recorded as mode M1,  $A_k$ ,  $\omega_k$ ,  $B_k$  and  $C_k$  are the coefficients of the model, additional numerical subscripts are used to distinguish different time periods.  $T_{flap}$  is the flapping period, noting that the initial flapping direction is upward.

For the second half cycle:

$$A_{f1}(t) = A_{k2} \sin(\omega_{k2}t + B_{k2}) - C_{k2}, \quad t \in [ T_{flap}/2, T_{flap} ) \tag{2}$$

Consider the pitch angle of the wing:

$$A_{b1}(t) = \begin{cases} \theta_{up}, & t \in [0, T_{flap}/4) \cup [3T_{flap}/4, T_{flap}) \\ \theta_{down}, & t \in [T_{flap}/4, 3T_{flap}/4) \end{cases} \tag{3}$$

where  $\theta_{up}$  is the pitch angle of the wing when it flutters upward,  $\theta_{down}$  is the pitch angle of the wing when it flutters down.

When the flapping wing aircraft flies in glide mode, the pitch angle and flapping angle of the wing can be maintained at a fixed value:

$$A_{b1} = \theta_0, \quad \theta_0 \in [0, \theta_m] \tag{4}$$

$$A_{f1} = \varphi_0, \quad \varphi_0 \in [0, \varphi_m] \tag{5}$$

where  $\theta_0$  is a given pitch angle,  $\theta_m$  is the boundary value of the pitch angle,  $\varphi_0$  is a given flapping angle,  $\varphi_m$  is the boundary value of the flapping angle. This glide mode is recorded as mode M0. Refer to Figure A1 for RCS results comparison of different wing shapes in the current mode.

### 2.2. Dynamic Electromagnetic Scattering

In the face of the same incident wave, the flapping of the wing causes the change of the position vector of any point on its surface, which leads to the change of the corresponding magnetic vector position:

$$A(\mathbf{r}) = \frac{\mu}{4\pi} \iint_{S_I(t)} \mathbf{J}_s(\mathbf{r}') \frac{e^{-jkR}}{R} dS \tag{6}$$

where  $A(\mathbf{r})$  is the magnetic vector position generated by the surface induced current,  $\mu$  is the permeability coefficient,  $\mathbf{J}_s$  is the induced current on the target surface,  $\mathbf{r}'$  is the coordinate vector of the source point,  $S_I(t)$  is the illumination area on the target surface,  $\mathbf{r}$  is the coordinate vector of the field point,  $k$  is the wave number in free space,  $dS$  is the integral facet, and  $R$  is the distance between the field point and the source point.

For the whole aircraft at any moment:

$$\mathbf{M}(m_{\text{flap}}(t)) = [\mathbf{M}(S_I(t)), \mathbf{M}(S_D(t))] \tag{7}$$

where  $\mathbf{M}$  represents grid coordinate matrix,  $m_{\text{flap}}$  is the model of the flapping wing aircraft,  $S_D(t)$  is the dark area on the target surface.

The electric and magnetic fields could be calculated according to the magnetic vector position:

$$\mathbf{E}(\mathbf{r}) = \frac{1}{j\omega\epsilon \cdot 4\pi} \iint_{S_I(t)} \left[ \frac{3 - k^2R^2 + j3kR}{R^5} e^{-jkR} \mathbf{R} \times (\mathbf{R} \times \mathbf{J}_s(\mathbf{r}')) + 2\mathbf{J}_s(\mathbf{r}') \frac{1 + jkR}{R^3} e^{-jkR} \right] dS \tag{8}$$

$$\mathbf{H}(\mathbf{r}) = \frac{1}{4\pi} \iint_{S_I(t)} \frac{-1 - jkR}{R^3} e^{-jkR} (\mathbf{R} \times \mathbf{J}_s(\mathbf{r}')) dS \tag{9}$$

where  $\omega$  is the electromagnetic wave angular frequency,  $\mathbf{R}$  is the distance vector between the field point and the source point, and  $\epsilon$  is the dielectric permittivity.

The surface of the flapping wing aircraft is discretized by triangular facets:

$$\mathbf{M}_{\text{flap}}(t = 0) = [\mathbf{M}_{w1}(t = 0), \mathbf{M}_{w2}(t = 0), \mathbf{M}_b(t = 0)] \tag{10}$$

where  $\mathbf{M}_{\text{flap}}$  is the grid coordinate matrix of the flapping wing aircraft,  $\mathbf{M}_{w1}$  is the grid coordinate matrix of the wing 1,  $\mathbf{M}_{w2}$  is the grid coordinate matrix of the wing 2,  $\mathbf{M}_b$  is the grid coordinate matrix of the aircraft body.

For any facet ( $F_{w1}$ ) on the surface of wing 1 when the wing starts pitching or flapping, the deflection effect of the facet on a given radar wave will change as shown in Figure 2, where  $F_b$  is the facet on the aircraft body.

For any vertex ( $P_i$ ) on any facet of the wing 1, its coordinate information will continuously change as the wing pitches when treating the wing as a rigid body:

$$\forall P_i = [x(P_i), y(P_i), z(P_i)]^T \in F_{w1} | i = 1, 2, \dots, N_{f,w1} \tag{11}$$

$$\forall F_{w1} \in \mathbf{M}_{w1}(t = 0) \tag{12}$$

$$\mathbf{M}(F_{w1}(A_p, t)) = \begin{bmatrix} 1 & 0 & 0 \\ 0 & \cos A_{p1}(t) & -\sin A_{p1}(t) \\ 0 & \sin A_{p1}(t) & \cos A_{p1}(t) \end{bmatrix} \cdot \mathbf{M}(F_{w1}(t = 0)) \tag{13}$$

where  $N_{f,w1}$  is the number of facets of the wing 1. Then consider the flapping of the wing:

$$\mathbf{M}(F_{w1}(A_f, A_p, t)) = \begin{bmatrix} 1 & 0 & 0 \\ 0 & \cos A_{f1}(t) & -\sin A_{f1}(t) \\ 0 & \sin A_{f1}(t) & \cos A_{f1}(t) \end{bmatrix} \cdot \mathbf{M}^y(F_{w1}(A_p, t)) \tag{14}$$

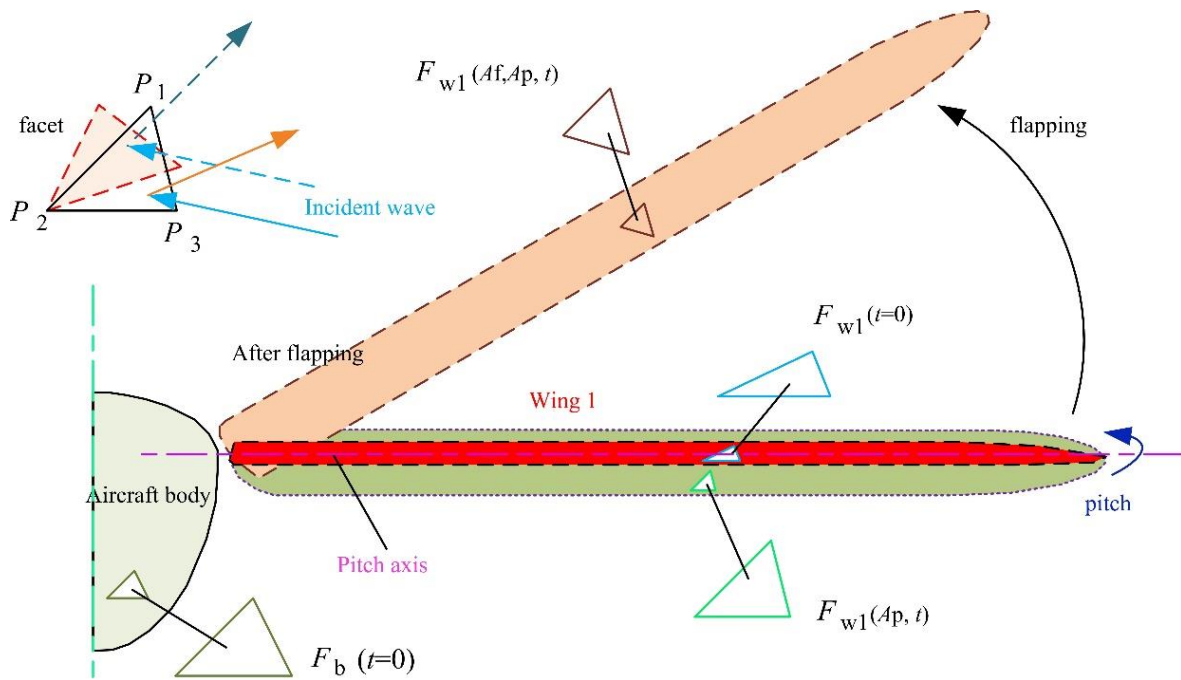


Figure 2. Schematic diagram of the facets in lighting area when wing flapping.

Noting the relationship between the flapping axis of the wing and the  $xz$  plane:

$$M^y(F_{w1}(A_p, t)) = M(y(F_{w1}(A_p, t)) - Y_{w1}) \tag{15}$$

where  $Y_{w1}$  is the distance from the flapping axis of the wing 1 to the  $xz$  plane. The flapping axis of the wing is parallel to the  $x$  axis and in the  $xy$  plane. The facet on the surface of wing 2 is treated similarly as above, thus the grid matrix of the whole flapping wing aircraft could be updated to:

$$M_{flap}(t) = [M_{w1}(t), M_{w2}(t), M_b(t)] \tag{16}$$

Therefore, the illumination area ( $S_I$ ) on the surface of the flapping wing aircraft can be dynamically generated. When the fuselage is always fixed in the current coordinate system:

$$M_{flap}(t) = [M_{w1}(t), M_{w2}(t), M_b(t = 0)] \tag{17}$$

According to the assumption of physical optics method, no current is generated on the facet in the unlighted area:

$$J_s = \begin{cases} 2\mathbf{n} \times \mathbf{H}, & S_I \\ \mathbf{0}, & S_D \end{cases} \tag{18}$$

where  $\mathbf{n}$  is the unit normal vector of the outer direction of  $\mathbf{r}'$  at the target surface. Then the electric field formula can be transformed to the following form:

$$\mathbf{E}(\mathbf{r}) = \frac{j}{\lambda r} |E_0| e^{-jk \cdot r} \iint_{S_I(t)} \hat{\mathbf{r}} \times \{ \hat{\mathbf{r}} \times [(\hat{\mathbf{n}}(\mathbf{r}') \cdot \mathbf{E}_0) \hat{\mathbf{k}} - (\hat{\mathbf{n}}(\mathbf{r}') \cdot \hat{\mathbf{k}}) \mathbf{E}_0] \} e^{-jk(-\hat{\mathbf{r}} + \hat{\mathbf{k}}) \cdot \mathbf{r}'} dS \tag{19}$$

where  $\lambda$  is the wavelength in free space,  $\mathbf{k}$  is the wave vector,  $r$  is the distance from the field point to the origin of coordinates. The integral term could be recorded as:

$$I(t) = \iint_{S_I(t)} \hat{\mathbf{r}} \times \{ \hat{\mathbf{r}} \times [(\hat{\mathbf{n}}(\mathbf{r}') \cdot \mathbf{E}_0) \hat{\mathbf{k}} - (\hat{\mathbf{n}}(\mathbf{r}') \cdot \hat{\mathbf{k}}) \mathbf{E}_0] \} e^{-jk(-\hat{\mathbf{r}} + \hat{\mathbf{k}}) \cdot \mathbf{r}'} dS \tag{20}$$

Then the dynamic RCS calculated by the physical optics method can be written as:

$$\sigma_F(t) = \frac{4\pi}{\lambda^2} |I(t)|^2 \tag{21}$$

where  $\sigma$  is the radar cross-section, subscript F represents the facet contribution. In fact, the flapping wing aircraft has many edge features, including the edge of the tail, the leading edge and trailing edge of the wing. Therefore, the contribution of edge diffraction cannot be ignored, thus physical theory of diffraction (PTD) is used to calculate the RCS contribution of the edge:

$$\sigma(t) = \left| \sum_{i=1}^{N_F(t)} \left( \sqrt{\sigma_F(t)} \right)_i + \sum_{j=1}^{N_E(t)} \left( \sqrt{\sigma_E(t)} \right)_j \right|^2, \quad t \in [0, T_{obs}] \tag{22}$$

where RCS subscript E represents the edge contribution.  $N_F$  is the number of facets,  $N_E$  is the number of edges.  $T_{obs}$  is the observation time boundary:

$$T_{obs} \geq T_{flap} \tag{23}$$

This time condition is set to ensure that the observed RCS curve can show changes in at least one flapping cycle. In addition, more RCS equations can refer to Equations (A1)–(A3), and the comparison of relevant results can refer to Figures A1 and A2.

### 2.3. Method Validation

The verification of the presented calculation method is shown in Figure 3, where PO + MOM (method of moment)/MLFMM (multilayer fast multipole method) in FEKO is used to calculate the RCS curve of the target in a given state. QSP is used to generate the pitch angle and flapping angle of the wing in the given discrete state. It can be found that the two RCS curves are generally similar, including shape, peak and mean level, where the RCS mean of the presented calculation method is  $-18.3819 \text{ dBm}^2$ , that of the other curve is  $-17.9068 \text{ dBm}^2$ . When  $\alpha = 0^\circ$ , both RCS curves have peaks exceeding  $4.279 \text{ dBm}^2$ , because the surface near the leading edge of the wing, the arc of the outer end of the wing and the lower surface of the wing all provide more scattering contributions.

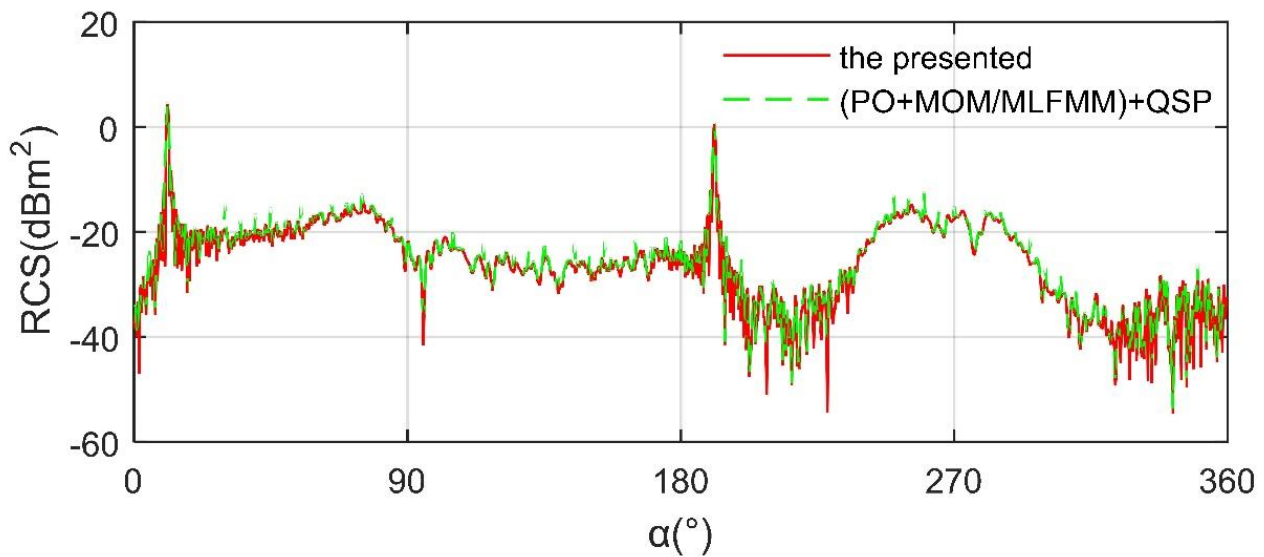


**Figure 3.** Verification of the presented calculation method on the wing 1,  $f_{th} = 7 \text{ GHz}$ ,  $t = 0.725 \text{ s}$ ,  $\beta = 0^\circ$ , mode M1,  $A_{k1} = C_{k1} = \pi/10$ ,  $\omega_{k1} = \omega_{k2} = 3.1416 \text{ rad/s}$ ,  $B_{k1} = B_{k2} = -\pi/2$ ,  $\theta_{up} = -\theta_{down} = 20^\circ$ ,  $A_{k2} = C_{k2} = \pi/12$ .

Noting that at  $t = 0.725$  s, the flapping angle of the wing 1 is  $29.6901^\circ$ , the pitch angle is  $20^\circ$ . When  $\alpha = 191^\circ$ , the RCS curve has the second largest peak, where the peak of the presented calculation method is  $0.5644 \text{ dBm}^2$ , that of the other is  $0.9483 \text{ dBm}^2$ . Other differences between the two curves are mainly reflected in local fluctuations. These results show that the presented calculation method is feasible to determine the RCS of the target.

### 3. Model of the Flapping-Wing Aircraft

The model of the flapping wing aircraft with two U-type wings is established as shown in Figure 4, where the wing 1 is marked red and wing 2 is marked green.  $L_b$  is the length of the aircraft body,  $L_t$  is the length of the aircraft tail,  $L_h$  is the length of the aircraft head,  $H_b$  is the height of the aircraft body.  $W_b$  is the width of the aircraft body,  $W_t$  is the width of the aircraft tail,  $W_{tn}$  is the minimum width of the fuselage tail. Airfoil 1 represents the airfoil used in the wing cross section. The aircraft model with bird wing shaped wings is built as shown in Figure A1.

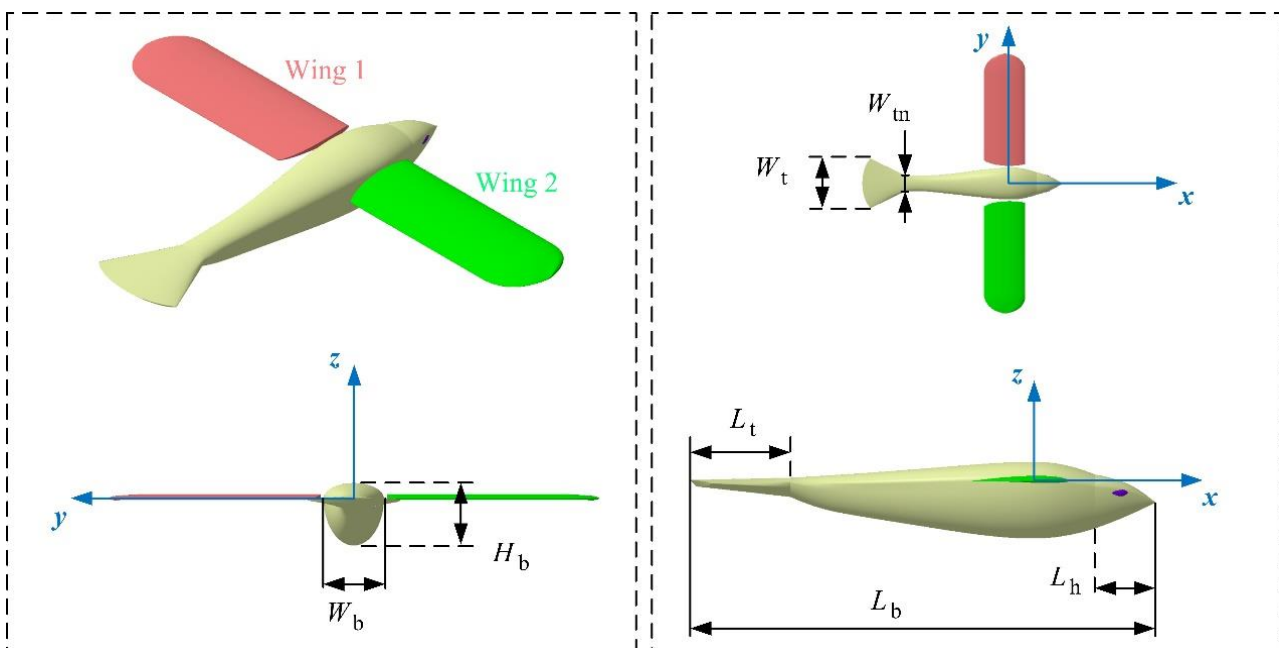


Figure 4. Modeling of the flapping wing aircraft with two U-shaped wings.

The parameter values of the flapping wing aircraft are shown in Table 1, where the wing 1 and wing 2 use the same shape design parameters. The fuselage curve is streamlined, and the plane contour of the tail presents a sector. The flapping axis of the wing is parallel to the  $x$ -axis and attached to the side of the airframe. At the initial moment, the pitch angle and flapping angle of the wing are equal to 0, where the pitch axis of the wing coincides with the  $y$ -axis.

Table 1. Parameter of the flapping wing aircraft.

Parameter	$L_b$ (m)	$L_t$ (m)	$L_h$ (m)	$H_b$ (m)
Value	3.657	0.787	0.47	0.6
Parameter	$W_b$ (m)	$W_t$ (m)	$W_{tn}$ (m)	Airfoil 1
Value	0.58	0.897	0.29	Uplink DLG

The details of the U-type wing are shown in Figure 5, where the plane profile of the wing is U-shaped, and the wing root is cut by curve.  $L_{w1}$  is the length of the wing,  $Y_{w1r}$  represents the distance from the wing root to the  $xz$  plane.  $Y_{u1}$  and  $Y_{u2}$  represent the distance at different spanwise sections of the U-type wing,  $C_{u1}$  and  $C_{u2}$  represent the chord

lengths at different sections of the U-arc wing.  $C_{w1}$  represents the chord length of the straight section of the U-type wing,  $X_{wle}$  represents the distance from the leading edge to the  $yz$  plane when the wing is placed horizontally.

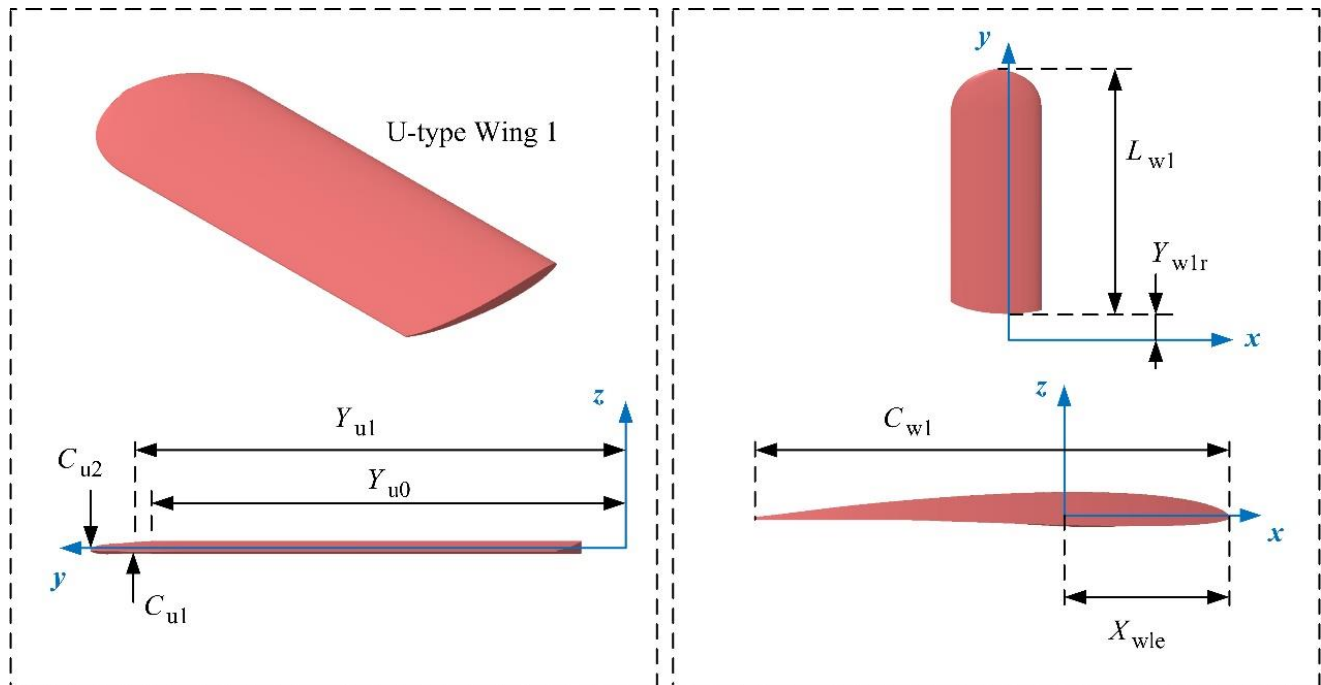


Figure 5. Details of the U-type wing model.

The values of wing parameters are shown in Table 2, where the straight section wing occupies the main part of the wing. For the wing part of U-shaped arc segment, the airfoil adopts affine operation to control the change of chord length. For the whole wing, there is no preset twist angle for each section when it is at the initial time.

Table 2. Parameter of the U-type wing.

Parameter	$L_{w1}$ (m)	$C_{w1}$ (m)	$Y_{w1r}$ (m)	$X_{w1e}$ (m)
Value	2.04	0.76	0.32	0.29
Parameter	$C_{u1}$ (m)	$C_{u2}$ (m)	$Y_{u0}$ (m)	$Y_{u1}$ (m)
Value	0.698	0.049	2	2.15

The grid of the flapping wing aircraft is generated as shown in Figure 6, where high precision unstructured mesh technology is used to discretize the surface of the model. The grid of wing 1 is still marked red and the grid of wing 2 is marked green. For those regions with small size or large curvature change, the grid density increase technique is implemented, such as the leading edge of the wing, the narrow surface region near the trailing edge of the wing, the edge of the tail, and the edge line of the fuselage.

The size distribution used for meshing is shown in Table 3, where the global minimum size is used to improve the mesh quality of the complex geometric features of the whole aircraft surface. For the connection between the straight section and U-arc section of the wing, the grid density increase technology is also adopted.

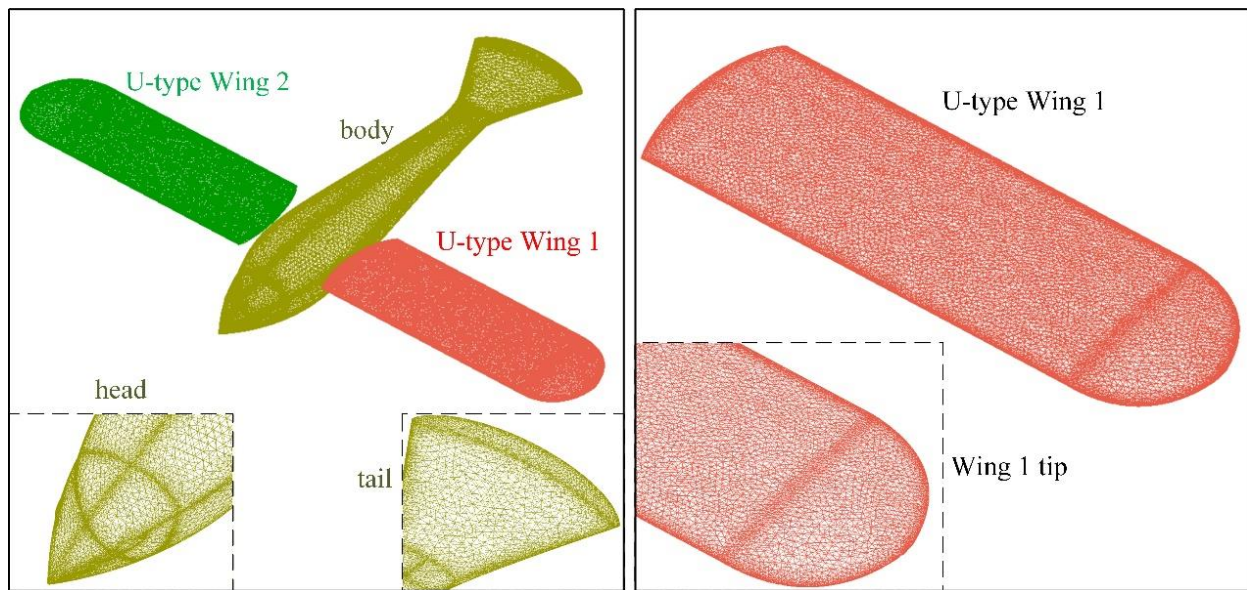


Figure 6. Grid of the flapping wing aircraft.

Table 3. Grid size of the flapping wing aircraft.

Region	Max Size (mm)	Region	Max Size (mm)
Global minimum size	1	Trailing edge of wing	2
Leading edge of wing	3	Wing tip airfoil	2
Wing tip edge	3	Tail edge	5
Head edge	10	Wing tip surface	15
Wing	25	Aircraft body	55

#### 4. Results and Discussion

##### 4.1. Influence of Frequency

Figure 7 provides that the increase of radar wave frequency will have a wide impact on the RCS curve of the flapping wing aircraft at a given observation angle, including variation range, local fluctuation, mean and peak value. For the RCS at 3 GHz, the curve varies from  $-26.73 \text{ dBm}^2$  to  $-14.6152 \text{ dBm}^2$ , where the RCS mean is  $-19.3432 \text{ dBm}^2$  as in Table 4. The minimum of RCS curve at 5 GHz is  $-33.16 \text{ dBm}^2$ , that of the RCS curve at 7 GHz is  $-35.16 \text{ dBm}^2$ . As the frequency of the incident wave increases from 3 GHz to 7 GHz, the mean value of the RCS curve of the aircraft at the given observation azimuth increases first and then decreases. For the case at 9 GHz, the minimum value of RCS curve is  $-30.76 \text{ dBm}^2$ . With the increase of radar wave frequency to 13 GHz, the maximum of RCS curve increases, while the mean value first decreases and then increases. In addition, the minimum value of the RCS curve at 11 GHz and 13 GHz is less than  $-33.55 \text{ dBm}^2$ . These results show that the influence of incident wave frequency on the dynamic RCS curve of the aircraft is mainly reflected in the peak and fluctuation range at the given observation angle.

Table 4. RCS mean and peak of the flapping wing aircraft, mode M1,  $A_{k1} = C_{k1} = \pi/10$ ,  $\omega_{k1} = \omega_{k2} = 3.1416 \text{ rad/s}$ ,  $B_{k1} = B_{k2} = -\pi/2$ ,  $\theta_{\text{up}} = -\theta_{\text{down}} = 20^\circ$ ,  $A_{k2} = C_{k2} = \pi/12$ ,  $\beta = 0^\circ$ ,  $\alpha = 29^\circ$ , RCS unit:  $\text{dBm}^2$ .

$f_{\text{rh}}$ (GHz)	3	5	7	9	11	13
Mean	-19.3432	-18.5952	-21.8308	-21.3989	-22.7407	-22.3742
Peak	-14.6152	-14.2637	-16.9687	-17.6932	-16.9422	-14.732

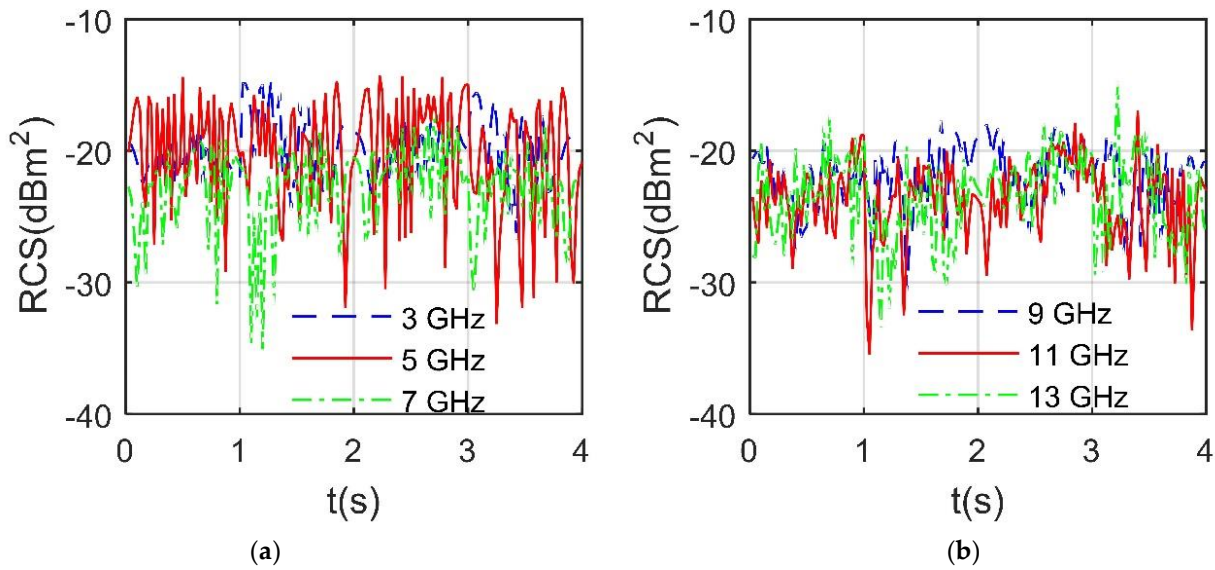


**Figure 7.** RCS of the flapping wing aircraft, mode M1,  $A_{k1} = C_{k1} = \pi/10$ ,  $\omega_{k1} = \omega_{k2} = 3.1416$  rad/s,  $B_{k1} = B_{k2} = -\pi/2$ ,  $\theta_{up} = -\theta_{down} = 20^\circ$ ,  $A_{k2} = C_{k2} = \pi/12$ ,  $\beta = 0^\circ$ ,  $\alpha = 29^\circ$ . (a) RCS at 3, 5, 7 GHz. (b) RCS at 9, 11, 13 GHz.

As shown in Figure 8a, the peak value of RCS curve at 2 GHz is higher than that of the other two curves, where the RCS curve at 2 GHz varies from  $-23.09$  dBm<sup>2</sup> to  $-9.224$  dBm<sup>2</sup>. The maximum value of RCS curve at 4 GHz is  $-10.1355$  dBm<sup>2</sup>, that of RCS curve at 6 GHz is  $-10.0856$  dBm<sup>2</sup>. This shows that in the current observation angle and frequency range, with the increase of frequency, the mean value of RCS curve first decreases and then increases, while the peak value decreases continuously. Noting that the RCS mean at 4 GHz is  $-15.291$  dBm<sup>2</sup>, that at 6 GHz is  $-14.6661$  dBm<sup>2</sup>. For the RCS at 8 GHz as in Figure 8b, the mean RCS is  $-17.9824$  dBm<sup>2</sup>, the peak is  $-12.3056$  dBm<sup>2</sup>. As the frequency of the incident wave increases to 12 GHz, the mean and peak of the RCS curve at that observation angle increase gradually, where the mean of the RCS curve at 10 GHz is  $-16.8794$  dBm<sup>2</sup>, that of the RCS curve at 12 GHz is  $-16.1253$  dBm<sup>2</sup>. When the radar wave frequency is 12 GHz, the maximum value of RCS curve reaches  $-11.3846$  dBm<sup>2</sup> and the minimum is  $-30.4$  dBm<sup>2</sup>. In addition, the shape and fluctuation of RCS curve change with the increase of frequency. These results show that under the current observation conditions, the increase of incident wave frequency will change the mean and peak level of RCS curve.

Figure 9 indicates that in the given M0 mode, the peak value of the RCS curve of the aircraft increases with the increase of the incident wave frequency. For the case of 2 GHz, the mean RCS of the curve is  $-0.5689$  dBm<sup>2</sup>, the peak is  $14.5160$  dBm<sup>2</sup>. When the incident wave frequency is 4 GHz, the mean value of RCS curve is equal to  $-0.9103$  dBm<sup>2</sup> and the peak value is  $15.4347$  dBm<sup>2</sup>. As the frequency increases to 4 GHz, the mean value of RCS curve further decreases to  $-1.2130$  dBm<sup>2</sup> and the peak value increases to  $15.7452$  dBm<sup>2</sup>. For a single RCS curve, two larger peaks can be found at azimuth angles equal to  $96.25^\circ$  and  $264.5^\circ$ , because at this time, the side surface of the aircraft body provides the main scattering contribution, and the outer end arc of the U-wing provides some scattering contribution. As the frequency further increases to 12 GHz, the mean value of RCS curve further decreases to  $-2.3674$  dBm<sup>2</sup>, and the peak value gradually increases to  $17.5255$  dBm<sup>2</sup>. In the current mode, the flapping wing aircraft remains in the gliding attitude, and the pitch angle and flapping angle of the wing remain unchanged. These results show that in the given M0 mode, the peak level of RCS curve increases gradually with the increase of incident wave frequency.

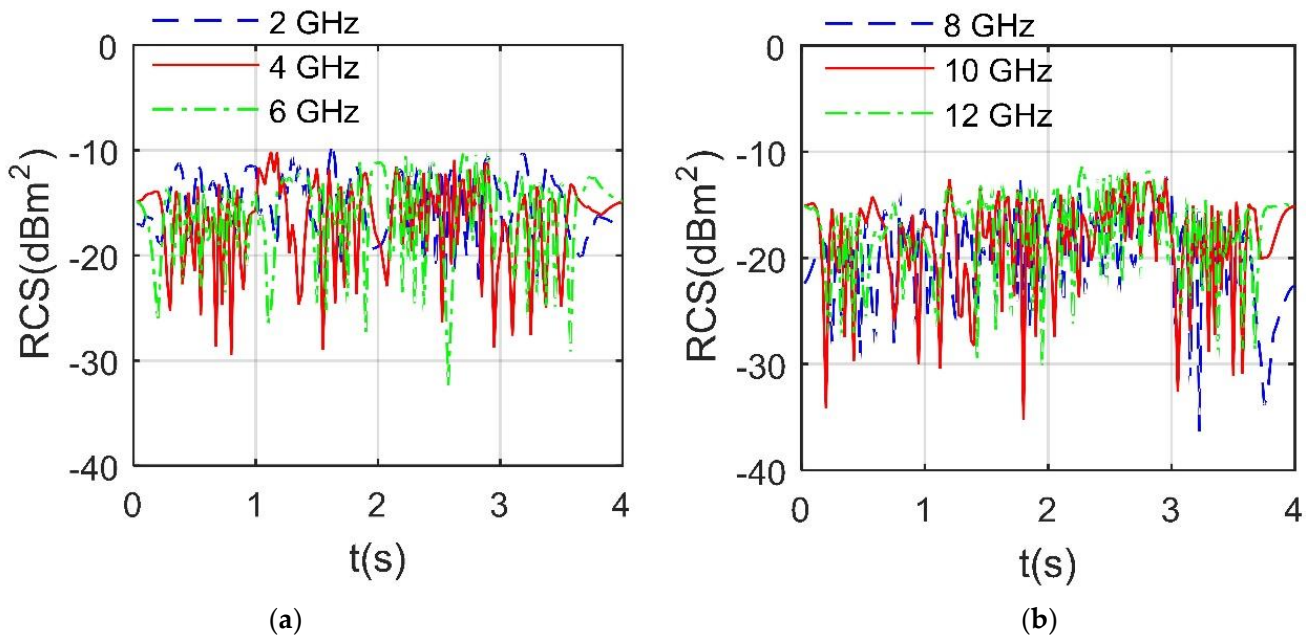


**Figure 8.** RCS of the flapping wing aircraft, mode M1,  $A_{k1} = C_{k1} = \pi/10$ ,  $\omega_{k1} = \omega_{k2} = 3.1416$  rad/s,  $B_{k1} = B_{k2} = -\pi/2$ ,  $\theta_{up} = -\theta_{down} = 20^\circ$ ,  $A_{k2} = C_{k2} = \pi/12$ ,  $\beta = 10^\circ$ ,  $\alpha = 50^\circ$ . (a) RCS at 2, 4, 6 GHz. (b) RCS at 8, 10, 12 GHz.

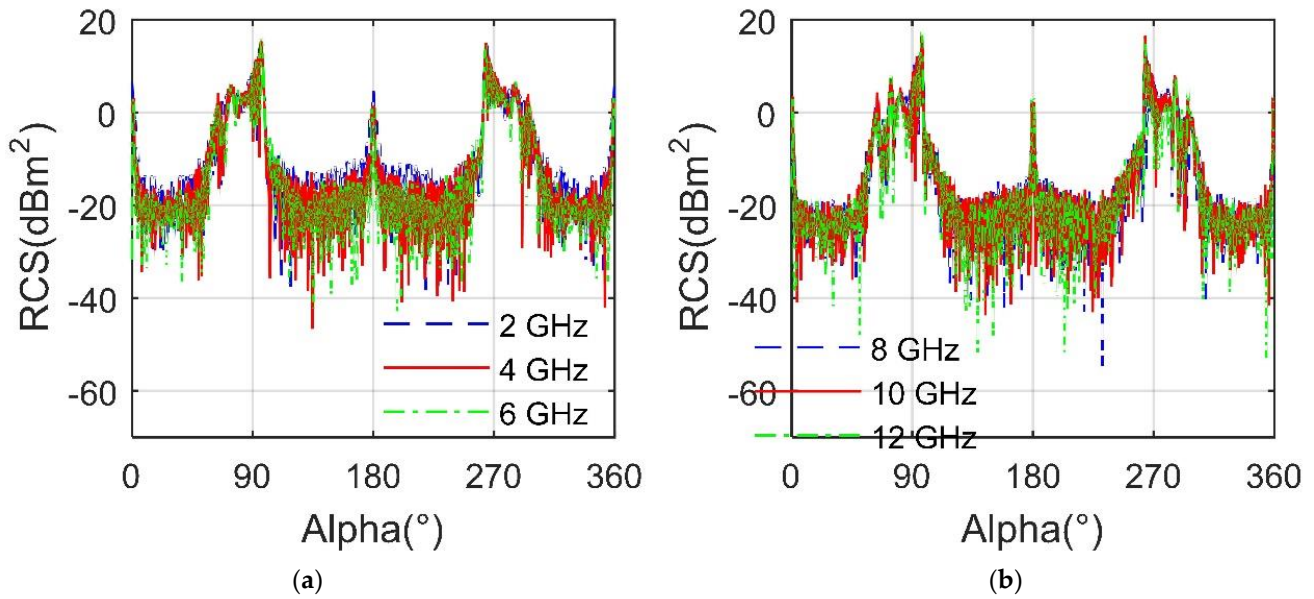


**Figure 9.** RCS of the flapping wing aircraft, mode M0,  $\theta_0 = 5^\circ$ ,  $\varphi_0 = 10^\circ$ ,  $\beta = 0^\circ$ . (a) RCS at 2, 4, 6 GHz. (b) RCS at 8, 10, 12 GHz.

4.2. Forward RCS Analysis

Figure 10 shows that in the given M1 mode, the RCS curve of the aircraft is obviously different under different forward azimuth. When  $\alpha = 0^\circ$ , the electromagnetic wave is incident in the negative direction along the  $x$ -axis, thus the leading edge of the wing and its adjacent surfaces are in the irradiation area.

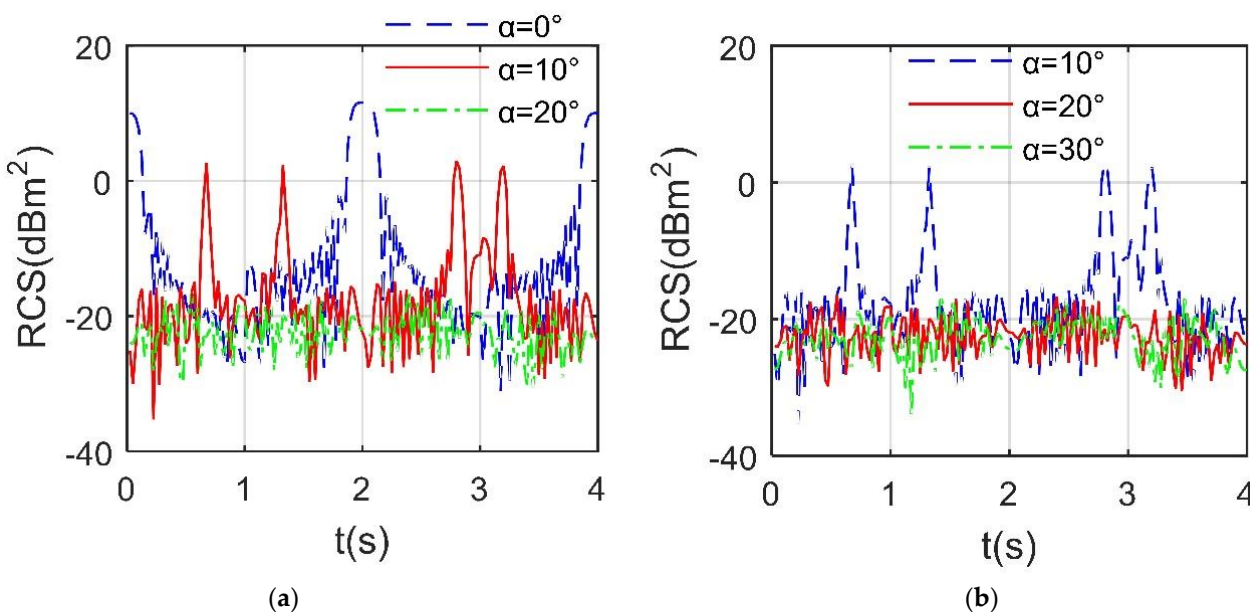


**Figure 10.** Forward RCS of the flapping wing aircraft, mode M1,  $A_{k1} = C_{k1} = \pi/10$ ,  $\omega_{k1} = \omega_{k2} = 3.1416$  rad/s,  $B_{k1} = B_{k2} = -\pi/2$ ,  $\theta_{up} = -\theta_{down} = 20^\circ$ ,  $A_{k2} = C_{k2} = \pi/12$ ,  $\beta = 0^\circ$ ,  $f_{th} = 7$  GHz. (a) RCS at  $\alpha = 0^\circ, 10^\circ, 20^\circ$ . (b) RCS at  $\alpha = 10^\circ, 20^\circ, 30^\circ$ .

With the wing pitching and flapping up and down, the RCS curve at  $0^\circ$  azimuth shows a trend of first decreasing, then increasing, then decreasing and then increasing with local fluctuations. The mean RCS of  $\alpha = 0^\circ$  curve is 1.3571 dBm<sup>2</sup>, the peak reaches 11.56 dBm<sup>2</sup>. As the azimuth increases to  $10^\circ$ , the mean level of RCS curve decreases rapidly to  $-9.6056$  dBm<sup>2</sup>, where the peak decreases to 2.9475 dBm<sup>2</sup>. At this time, the RCS curve shows four large peaks and some small local fluctuations. When  $\alpha = 20^\circ$ , the mean RCS of the curve is as low as  $-21.5189$  dBm<sup>2</sup>, and the peak value is reduced to  $-16.4791$  dBm<sup>2</sup>. As the azimuth angle further increases to  $30^\circ$ , the mean value of RCS curve decreases to  $-21.8629$  dBm<sup>2</sup> and the peak decreases to  $-16.4729$  dBm<sup>2</sup>. The peaks of RCS curves at  $0^\circ$  and  $10^\circ$  azimuth are significantly higher than those of the remaining two curves. As the azimuth increases from  $0^\circ$  to  $30^\circ$ , the peak value, mean value and fluctuation range of RCS curve decrease significantly. These results show that the mean and peak value of the forward RCS curve of the flapping wing aircraft will be lower at a large forward azimuth.

Figure 11 shows that under the given M1 mode, the electromagnetic scattering characteristics of the wing surface change obviously with the flapping of the wing. For the case at  $\alpha = 10^\circ$  and  $t = 0.5$  s, the flapping angle of the wing 1 is  $18^\circ$ , where the pitch angle of the wing is  $20^\circ$ . Because the electromagnetic wave is incident from the front and bottom direction of the wing, the leading edge of the wing presents a small number of yellow areas. The upper surface of the wing and the top area of the tail are dark blue, where a small amount of yellow and orange inclusions is distributed on the side of the body. There are many orange-red areas in the head of the body, and some edge and transition areas are yellow. The lower surface of wing 1 is orange red, while the lower surface of wing 2 is orange. For the case at  $\alpha = 20^\circ$  and  $t = 2.8$  s, the flapping angle of the wing 1 is  $27.1353^\circ$ , the pitch angle of the wing is  $-20^\circ$ . Since the absolute value of the pitch angle of the wing is greater than the elevation angle, all the upper surfaces of the wing 1 are illuminated. In addition to the effect of increasing azimuth, the leading edge of the upper surface of wing 2 and its adjacent half of the upper surface are illuminated. The dark blue area on the top of the body is enlarged, and the color depth of the red area on the side of the nose is slightly deepened. Since the wing is flapping downward, the scattering characteristics of the upper surface of wing 1 are strong. From the leading edge of wing 1 to the middle of wing 1, it presents an orange to yellow gradient. These results show that flapping wings will bring changing strong scattering sources to the flapping aircraft.

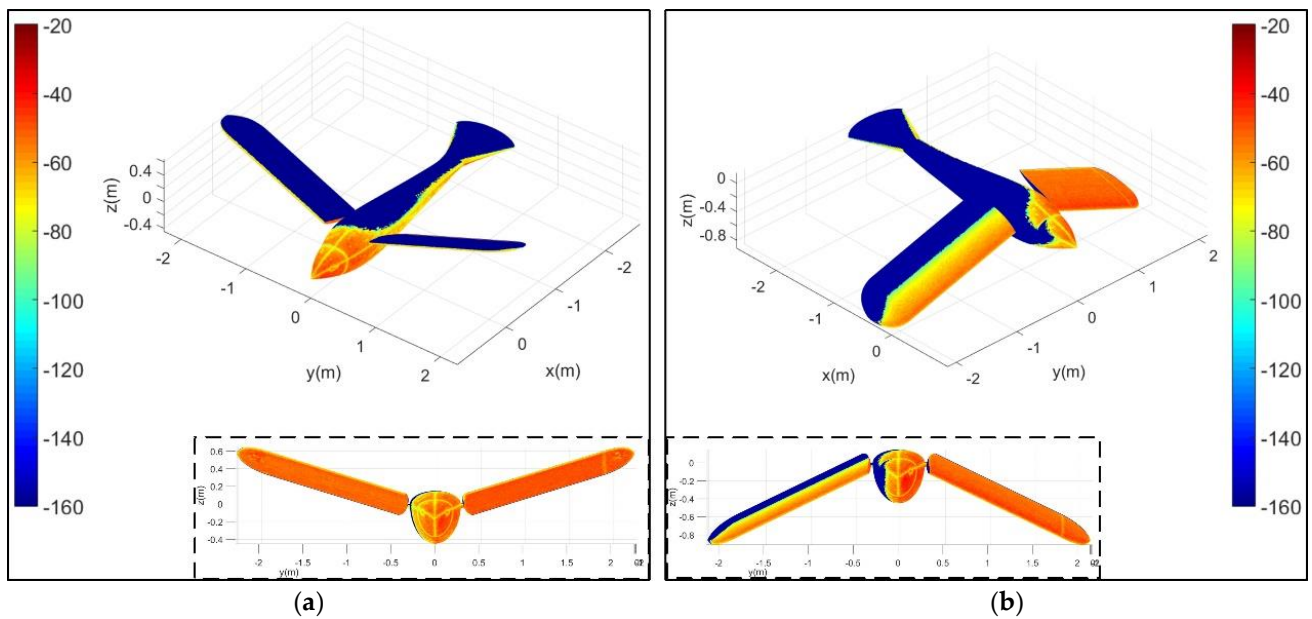


**Figure 11.** Surface scattering characteristics of the aircraft, mode M1,  $A_{k1} = C_{k1} = \pi/10$ ,  $\omega_{k1} = \omega_{k2} = 3.1416$  rad/s,  $B_{k1} = B_{k2} = -\pi/2$ ,  $\theta_{up} = -\theta_{down} = 20^\circ$ ,  $A_{k2} = C_{k2} = \pi/12$ ,  $\beta = -5^\circ$ ,  $f_{th} = 7$  GHz, RCS unit; dBm<sup>2</sup>. (a) Case at  $\alpha = 10^\circ$ ,  $t = 0.5$  s. (b) Case at  $\alpha = 20^\circ$ ,  $t = 2.8$  s.

As shown in Figure 12, the increase of elevation angle will have a significant impact on the RCS~azimuth curve of the flapping wing aircraft. For the RCS at  $\alpha = 0^\circ$ , the RCS curve with  $\beta = 20^\circ$  is significantly different from the other two RCS curves, including shape and peak value. Within 0 to 1 s, the RCS curve with  $\beta = 20^\circ$  fluctuates slightly near 9.813 dBm<sup>2</sup>, and the fluctuation here is displayed as a straight line within the current observation range. Because the elevation angle is equal to the pitch angle of the wing, the leading edge of the wing is the irradiation area, and the scattering level of the upper and lower surfaces of the wing is low. From 1 to 3 s, the wing starts to flap downward, while the pitch angle of the wing remains  $-20^\circ$ , making the upper surface of the wing a dynamic strong scattering source. The peak of the RCS curve at  $\beta = 20^\circ$  is 14.16 dBm<sup>2</sup>, that of the RCS curve at  $\beta = 10^\circ$  is 10.91 dBm<sup>2</sup>. The mean value of RCS curve with  $\beta = 20^\circ$  reaches 7.6523 dBm<sup>2</sup>, which makes the current observation conditions unfavorable for the stealth flight of the aircraft. For the RCS at  $\alpha = 20^\circ$ , as the elevation angle increases from  $0^\circ$  to  $20^\circ$ , the mean of RCS curve increases from  $-21.5189$  dBm<sup>2</sup> to  $-7.8321$  dBm<sup>2</sup>. The RCS curve with  $\beta = 10^\circ$  has a peak greater than 4.98 dBm<sup>2</sup>, while the RCS curve with  $\beta = 20^\circ$  has two peaks greater than 9.46 dBm<sup>2</sup>. These results show that under the forward azimuth, the increase of elevation angle will significantly change the dynamic RCS characteristics of the flapping wing aircraft, and increase the mean and peak levels.

#### 4.3. Side RCS Analysis

Figure 13 investigates that the mean value of RCS curve of the aircraft is different under different lateral azimuth. As the azimuth increases from  $40^\circ$  to  $60^\circ$ , the mean value of the RCS curve increases from  $-20.6414$  dBm<sup>2</sup> to  $-5.9584$  dBm<sup>2</sup>, the peak increases from  $-16.59$  dBm<sup>2</sup> to  $-3.3$  dBm<sup>2</sup>. When  $\alpha = 50^\circ$ , the mean of the RCS curve is  $-16.7467$  dBm<sup>2</sup>, where the fluctuation range is from  $-31.13$  dBm<sup>2</sup> to  $-12.3466$  dBm<sup>2</sup>. As the azimuth increases from  $60^\circ$  to  $80^\circ$ , the mean and peak values of RCS curves first decrease and then increase. When  $\alpha = 80^\circ$ , the mean value of the RCS curve is 2.1729 dBm<sup>2</sup>, where the peak is 4.0392 dBm<sup>2</sup>. In view of the increasing azimuth, the scattering contribution of the body side of the flapping wing aircraft gradually increases, which improves the mean level of the RCS curve. At the same time, the contribution of the dynamic scattering characteristics of the outer camber of the U-wing increases gradually, while the contribution of the leading edge of the wing decreases gradually.

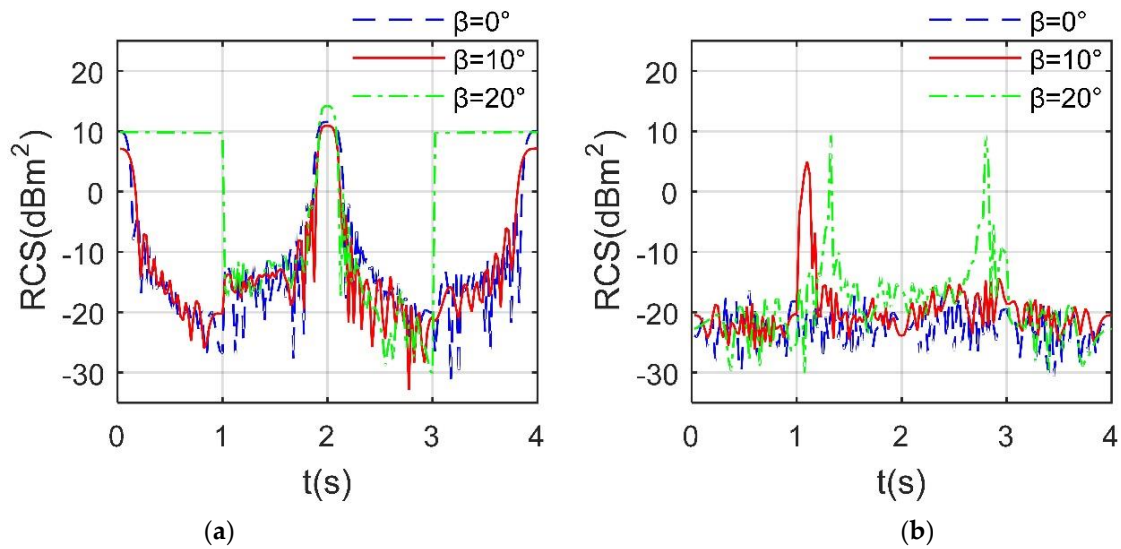


**Figure 12.** RCS of the flapping wing aircraft, mode M1,  $A_{k1} = C_{k1} = \pi/10$ ,  $\omega_{k1} = \omega_{k2} = 3.1416$  rad/s,  $B_{k1} = B_{k2} = -\pi/2$ ,  $\theta_{up} = -\theta_{down} = 20^\circ$ ,  $A_{k2} = C_{k2} = \pi/12$ ,  $f_{rh} = 7$  GHz. (a) RCS at  $\alpha = 0^\circ$ . (b) RCS at  $\alpha = 20^\circ$ .

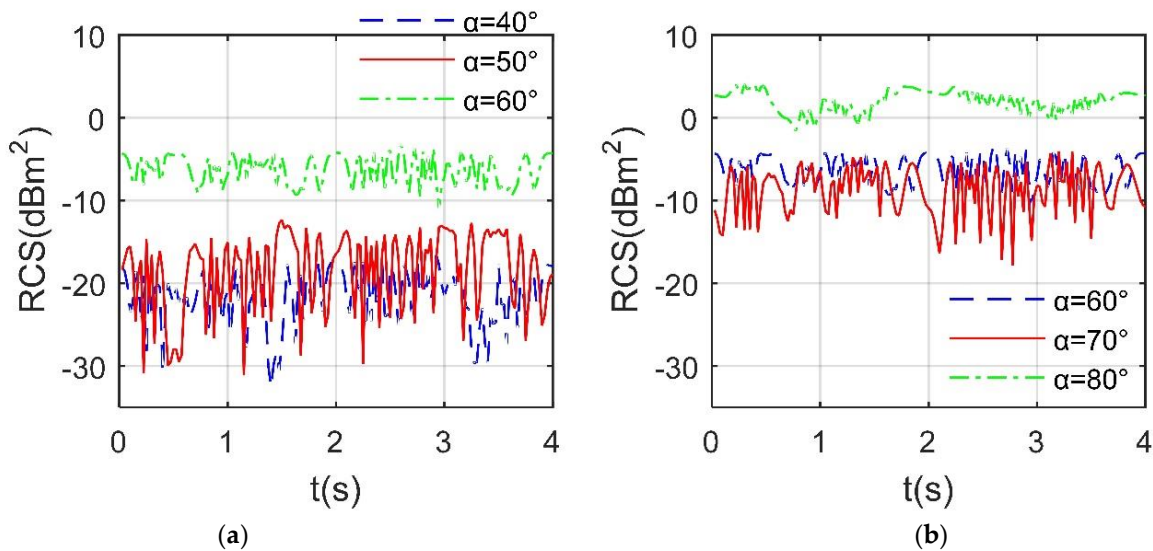


**Figure 13.** Side RCS of the flapping wing aircraft, mode M1,  $A_{k1} = C_{k1} = \pi/10$ ,  $\omega_{k1} = \omega_{k2} = 3.1416$  rad/s,  $B_{k1} = B_{k2} = -\pi/2$ ,  $\theta_{up} = -\theta_{down} = 20^\circ$ ,  $A_{k2} = C_{k2} = \pi/12$ ,  $\beta = 0^\circ$ ,  $f_{rh} = 7$  GHz. (a) RCS at  $\alpha = 40^\circ, 50^\circ, 60^\circ$ . (b) RCS at  $\alpha = 60^\circ, 70^\circ, 80^\circ$ .

As presented in Figure 14a, the shapes and peaks of the three RCS curves are different, where the peak of the curve at  $\alpha = 100^\circ$  is  $-6.4955$  dBm<sup>2</sup>, that of the curve at  $\alpha = 120^\circ$  is  $-17.6693$  dBm<sup>2</sup>. The mean value and fluctuation range of the two RCS curves with  $\alpha = 100^\circ$  and  $\alpha = 110^\circ$  are similar, where the mean of the former curve is  $-9.5172$  dBm<sup>2</sup>, that of the later curve is  $-11.7566$  dBm<sup>2</sup>. As the azimuth increases from  $100^\circ$  to  $120^\circ$ , the mean and peak of RCS curve show a decreasing trend, because the trailing edge of the wing and its adjacent surface become the main dynamic scattering source. Note that the trailing edge of the wing has thinner geometric features than the leading edge and outer end, resulting in lower scattering contribution. For the Figure 14b, it can be seen that the fluctuation ranges of the three RCS curves are similar. As the azimuth increases from  $130^\circ$  to  $150^\circ$ , the mean and peak value of RCS curve first increases and then decreases, where the mean of the curve at  $\alpha = 130^\circ$  is  $-23.0354$  dBm<sup>2</sup>, that of the curve at  $\alpha = 150^\circ$  is  $-21.8895$  dBm<sup>2</sup>. These results show that for the lateral backward azimuth, the mean value of the dynamic RCS

curve of the flapping wing aircraft generally decreases with the approach of the incident wave to the tail.

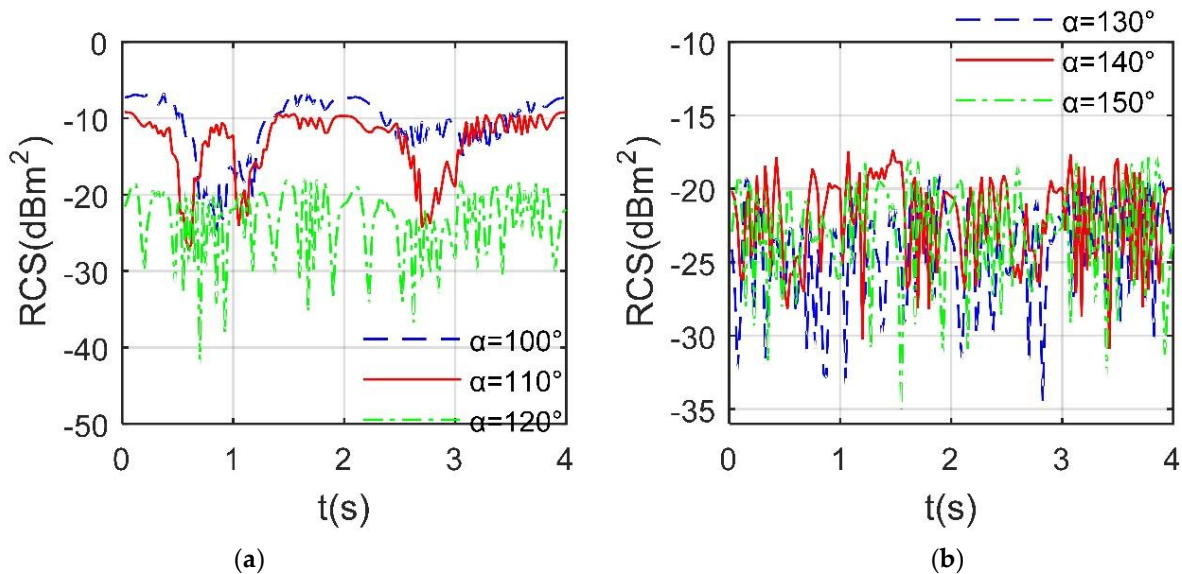


**Figure 14.** Side RCS of the flapping wing aircraft, mode M1,  $A_{k1} = C_{k1} = \pi/10$ ,  $\omega_{k1} = \omega_{k2} = 3.1416$  rad/s,  $B_{k1} = B_{k2} = -\pi/2$ ,  $\theta_{up} = -\theta_{down} = 20^\circ$ ,  $A_{k2} = C_{k2} = \pi/12$ ,  $f_{rh} = 7$  GHz,  $\beta = 0^\circ$ . (a) RCS at  $\alpha = 100^\circ, 110^\circ, 120^\circ$ . (b) RCS at  $\alpha = 130^\circ, 140^\circ, 150^\circ$ .

#### 4.4. Tail RCS Analysis

Figure 15 reveals that with the increase of azimuth, the peak level of RCS curve of flapping wing aircraft increases. For the RCS at  $\beta = 0^\circ$ , the mean of the RCS curve at  $\alpha = 160^\circ$  is  $-21.4583$  dBm<sup>2</sup>, that of the curve at  $\alpha = 170^\circ$  is  $-12.4488$  dBm<sup>2</sup>. As the azimuth increases to  $180^\circ$ , the mean value of RCS curve is increased to  $-3.3248$  dBm<sup>2</sup> and the peak value is increased to  $6.1166$  dBm<sup>2</sup>, because at this time, the trailing edge of the wing and its adjacent areas provide more dynamic scattering contributions, and the surface and edge of the aircraft tail provide more static scattering contributions. Compared with the forward RCS curve, the shape of the RCS curve at  $180^\circ$  azimuth is similar to that at  $0^\circ$  azimuth, while the peak and mean are lower. For the RCS at  $\alpha = 160^\circ$ , the RCS curves at different elevation angles have obvious differences in peak value and fluctuation range. As the elevation angle increases from  $0^\circ$  to  $20^\circ$ , the mean value of RCS curve increases from  $-21.4583$  dBm<sup>2</sup> to  $-15.9451$  dBm<sup>2</sup>, where the peak value increases from  $-17.0297$  dBm<sup>2</sup> to  $0.1886$  dBm<sup>2</sup>. At a large elevation angle, the U-shaped camber, trailing edge and upper surface of the wing can provide dynamic scattering sources. These results show that the peak value and mean value of the aircraft RCS curve increase with the increase of azimuth within a given range of tail azimuth.

As shown in Figure 16a, under the given observation azimuth, the peak levels of the three RCS curves are similar. The mean RCS of the curve at  $\beta = 0^\circ$  is  $-12.4488$  dBm<sup>2</sup>, that of the curve at  $\beta = 10^\circ$  is  $-15.939$  dBm<sup>2</sup>. As the elevation angle increases from  $0^\circ$  to  $20^\circ$ , the peak of RCS curve decreases from  $0.2447$  dBm<sup>2</sup> to  $-2.0169$  dBm<sup>2</sup>, and the mean value decreases from  $-12.4488$  dBm<sup>2</sup> to  $-17.0115$  dBm<sup>2</sup>. In addition, the RCS curve with  $\beta = 0^\circ$  has four large peaks, while the other two curves have two large peaks. For the Figure 16b, it can be found that the shape of RCS curve changes greatly when  $\beta = 20^\circ$ . Although the peaks of the three RCS curves are around  $6.25$  dBm<sup>2</sup>, their mean values are different. The mean of the RCS curve at  $\beta = 0^\circ$  is  $-3.3248$  dBm<sup>2</sup>, that of the curve at  $\beta = 10^\circ$  is  $-2.8461$  dBm<sup>2</sup>, where the fluctuation range and trend of the two RCS curves are similar. When  $\beta = 20^\circ$ , the RCS curve has a wide range of values higher than  $1.025$  dBm<sup>2</sup> in the middle period, because at this time, the two U-shaped wings are flapping downward, and the trailing edge of the wing has been providing a large scattering contribution. These results show that in

the positive tail direction ( $\alpha = 180^\circ$ ), the increase of lift angle is unfavorable to the peak and mean of the dynamic RCS curve of the flapping wing aircraft.

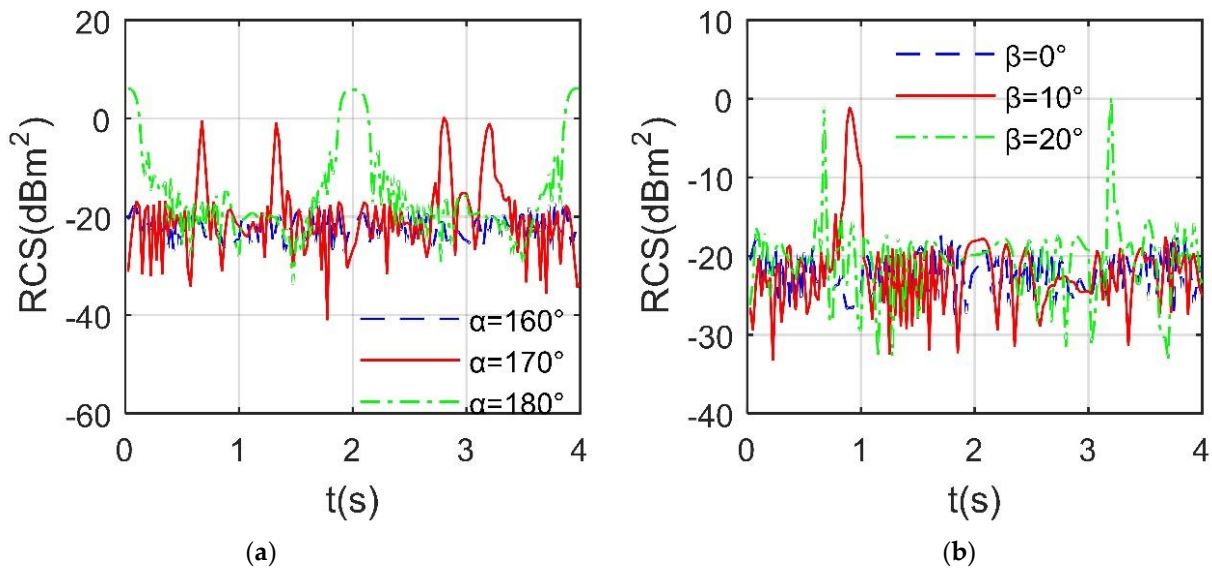


**Figure 15.** Tail RCS of the flapping wing aircraft, mode M1,  $A_{k1} = C_{k1} = \pi/10$ ,  $\omega_{k1} = \omega_{k2} = 3.1416$  rad/s,  $B_{k1} = B_{k2} = -\pi/2$ ,  $\theta_{up} = -\theta_{down} = 20^\circ$ ,  $A_{k2} = C_{k2} = \pi/12$ ,  $f_{rh} = 7$  GHz. (a) RCS at  $\beta = 0^\circ$ . (b) RCS at  $\alpha = 160^\circ$ .

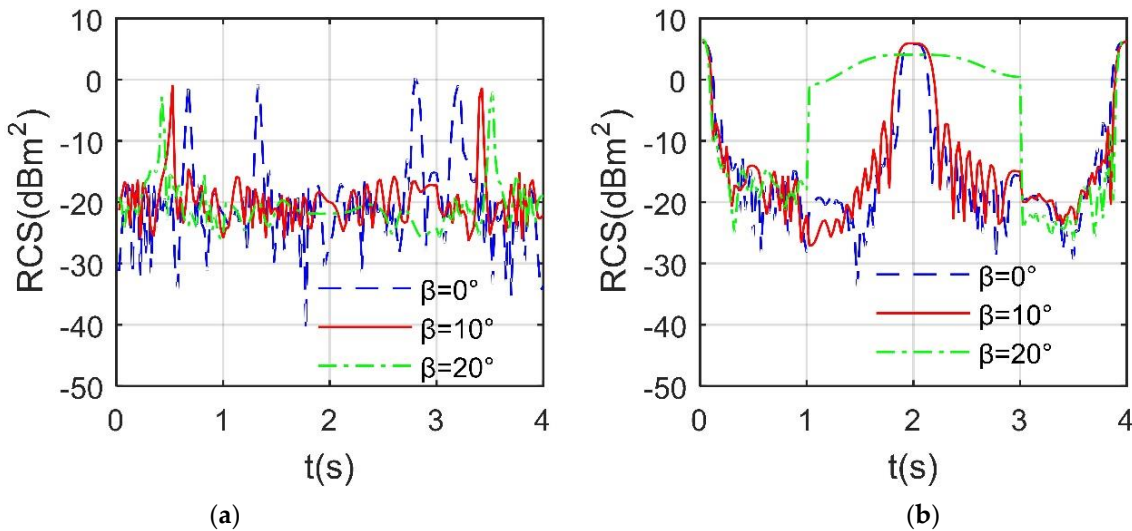


**Figure 16.** Tail RCS of the flapping wing aircraft, mode M1,  $A_{k1} = C_{k1} = \pi/10$ ,  $\omega_{k1} = \omega_{k2} = 3.1416$  rad/s,  $B_{k1} = B_{k2} = -\pi/2$ ,  $\theta_{up} = -\theta_{down} = 20^\circ$ ,  $A_{k2} = C_{k2} = \pi/12$ ,  $f_{rh} = 7$  GHz. (a) RCS at  $\alpha = 170^\circ$ . (b) RCS at  $\alpha = 180^\circ$ .

### 5. Conclusions

Based on the established dynamic scattering method, the electromagnetic scattering characteristics of the U-type flapping wing aircraft are studied. Through the analysis and discussion, this paper can draw the following conclusions:

- (1) In the given gliding mode, the peak of the RCS curve of the aircraft increases with the increase of the radar wave frequency while the fuselage provides more contribution to lateral RCS peak. In the given flapping mode, the frequency mainly affects the local fluctuation of the aircraft dynamic RCS curve.
- (2) For the given forward azimuth range in flapping mode, increasing the azimuth can reduce the mean and peak levels of the aircraft dynamic RCS curve, while increasing

the elevation angle will increase the peak and mean levels of the aircraft dynamic RCS curve.

- (3) In the flapping mode, the mean of the dynamic RCS curve of the aircraft in the lateral backward azimuth is significantly lower than that in the lateral forward azimuth. For the given tail azimuth range, the increase of azimuth will increase the mean and peak of aircraft dynamic RCS curve.

Future outlook: two segment wing, multi segment wing and elastic wing will be the focus of research. Practical flapping control law and attitude change also need more attention.

**Author Contributions:** Conceptualization, Z.Z. and J.H.; methodology and validation, Z.Z.; formal analysis, investigation, Z.Z. and J.H.; writing—original draft preparation, Z.Z.; writing—review and editing, Z.Z. and J.H.; visualization, funding acquisition, Z.Z. All authors have read and agreed to the published version of the manuscript.

**Funding:** This research was supported by the project funded by China Postdoctoral Science Foundation (Grant Nos. BX20200035, 2020M680005).

**Institutional Review Board Statement:** Not applicable.

**Informed Consent Statement:** Not applicable.

**Data Availability Statement:** Not applicable.

**Acknowledgments:** Thanks to Jun Huang for his guidance on the study work of this paper.

**Conflicts of Interest:** The authors declare no conflict of interest.

### Appendix A. Wing Shape and Multiple Scattering

A flapping wing aircraft model with reference to the shape of bird wings has been established as shown in Figure A1, where  $M_{f1}$  represents the aircraft with U-shaped wings, and  $M_{f2}$  represents the aircraft with plane shape of bird wing, noting that the airfoil and fuselage of these two types of aircraft are the same, and the  $M_{f2}$  wingspan is 5.296 m. The RCS mean of  $M_{f1}$  curve is  $-2.5477$  dBm<sup>2</sup>, that of  $M_{f2}$  curve is  $-3.1651$  dBm<sup>2</sup>, showing that although there are small differences in the shape and span of wings, the average RCS levels of these two types of aircraft are close. The peak of  $M_{f1}$  curve is 14.15 dBm<sup>2</sup> appearing at 97° azimuth, that of  $M_{f2}$  curve is 15.31 dBm<sup>2</sup> at 97° azimuth, indicating that the peak levels of these two aircraft are similar. These results show that the RCS of these two aircraft with different wing shapes are similar in mean level and peak value, and the main difference is reflected in local maximum value and local fluctuation.

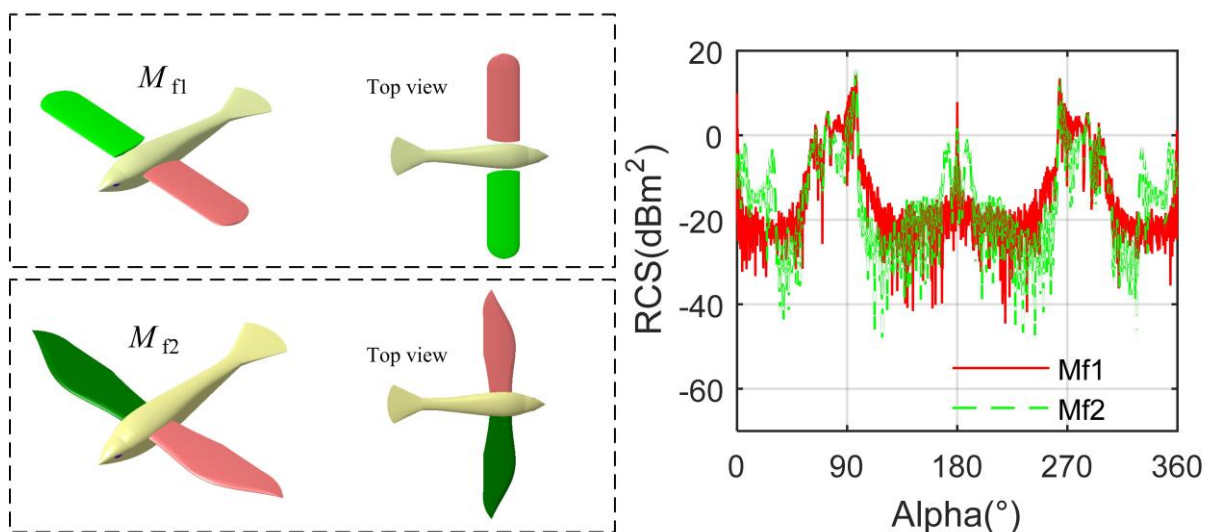


**Figure A1.** Comparison of different wing shapes, mode M0,  $\theta_0 = 0^\circ$ ,  $\varphi_0 = 0^\circ$ ,  $\beta = 2^\circ$ ,  $f_{rh} = 7$  GHz.

For electromagnetic waves under certain incident conditions, there may be secondary or multiple reflections on the target surface:

$$J_n(\mathbf{r}) = J_0(\mathbf{r}) + 2\hat{\mathbf{n}} \times \iint_S J_{n-1}(\mathbf{r}') \times \nabla' G(\mathbf{r}, \mathbf{r}') ds' \quad (\text{A1})$$

where  $J$  means the surface current, and the subscript means the scattering number.  $G$  is the Green function of free space:

$$G(\mathbf{r}, \mathbf{r}') = \frac{e^{-jk|\mathbf{r}-\mathbf{r}'|}}{4\pi|\mathbf{r}-\mathbf{r}'|} \quad (\text{A2})$$

Considering the current under irradiation, its expression can be updated to:

$$J_n(\mathbf{r}) = 2\hat{\mathbf{n}} \times \mathbf{H}_i(\mathbf{r}) + 2\hat{\mathbf{n}} \times \iint_S J_{n-1}(\mathbf{r}') \times \nabla' G(\mathbf{r}, \mathbf{r}') ds' \quad (\text{A3})$$

The RCS of  $M_{f2}$  aircraft considering multiple scattering is shown in Figure A2, where  $N_{ms}$  is the number of times of multiple scattering. The average RCS of  $N_{ms} = 1$  curve is  $-2.0732 \text{ dBm}^2$ , where the maximum is  $13.87 \text{ dBm}^2$  occurring at  $96^\circ$  azimuth. Under the current observation conditions, the mean RCS of the  $N_{ms} = 2$  curve is equal to  $-2.0732 \text{ dBm}^2$ , where the peak size and position remain unchanged, because the surface of this target adopts a concise shape design, which has a good deflection effect on the current incident wave. This performance can also be reflected in the remaining two curves. If it is necessary to obtain the obvious difference caused by multiple scattering, it is feasible to adjust the appropriate incidence angle.

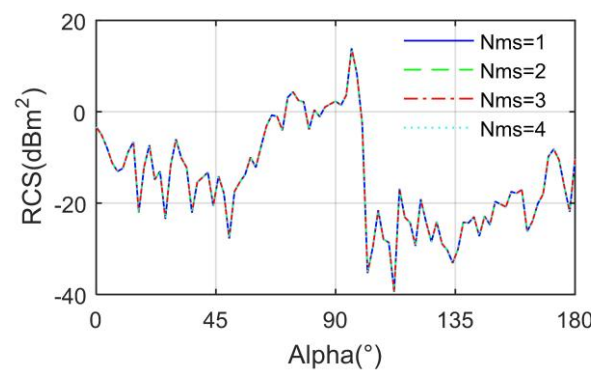


**Figure A2.** RCS of  $M_{f2}$  aircraft considering multiple scattering, mode M0,  $\theta_0 = 0^\circ$ ,  $\varphi_0 = 0^\circ$ ,  $\beta = 0^\circ$ ,  $f_{th} = 3 \text{ GHz}$ .

## References

- Shen, H.; Yu, Y. Development and key technologies of morphological bionic aircraft. *Adv. Aeronaut. Sci. Eng.* **2021**, *12*, 9–19.
- Bian, Z.; Li, J.; Guo, L.; Luo, X. Analyzing the Electromagnetic Scattering Characteristics of a Hypersonic Vehicle Based on the Inhomogeneity Zonal Medium Model. *IEEE Trans. Antennas Propag.* **2021**, *69*, 971–988. [[CrossRef](#)]
- Wu, J.; Li, Z. Study on the aerodynamic forces of flapping wing MAV with PVDF sensor. *Piezoelectrics Acousto-optics* **2012**, *34*, 712–715.
- Bluman, J.E.; Pohly, J.A.; Sridhar, M.K.; Kang, C.K.; Landrum, D.B.; Fahimi, F.; Aono, H. Achieving bioinspired flapping wing hovering flight solutions on Mars via wing scaling. *Bioinspiration Biomim.* **2018**, *13*, 046010. [[CrossRef](#)]
- Ang, H.; Zeng, R.; Duan, W.; Shi, Z. Aerodynamic experimental investigation for mechanism of lift and thrust of flexible flapping-wing MAV. *J. Aerosp. Power* **2007**, *22*, 1837–1844.
- Jiao, Z.; Wang, L.; Zhao, L.; Jiang, W. Hover flight control of X-shaped flapping wing aircraft considering wing–tail interactions. *Aerosp. Sci. Technol.* **2021**, *116*, 106870. [[CrossRef](#)]
- Cui, X.; Wei, R.; Zhou, X.; Shao, M.; Huang, J. Aerodynamic computation of flapping-wing simulation bird wings. *J. Syst. Simul.* **2009**, *21*, 4995–4998.
- Gueddida, A.; Djafari Rouhani, B.; Pennec, Y.; Di Donato, A.; Pierantoni, L.; Korovin, A.; Mencarelli, D. Coupling of Integrated Waveguide and Optomechanic Cavity for Microwave Phonon Excitation in Si Nanobeams. *Photonics* **2020**, *7*, 67. [[CrossRef](#)]

9. Zhang, Y.; Song, W.; Song, B.; Zhang, W. Research on wing structure deformation for aerodynamic force and inertial force of flapping-wing. *J. Aerosp. Power* **2010**, *25*, 1561–1566.
10. Abbasi, S.H.; Mahmood, A.; Khaliq, A. Bioinspired Feathered Flapping Wing UAV Design for Operation in Gusty Environment. *J. Robot.* **2021**, *2021*, 8923599. [[CrossRef](#)]
11. Bao, F.; Yang, Q.; He, Y. Experimental investigation on shedding vortex and lift mechanism of flapping wing model single degree of freedom. *J. Aerosp. Power* **2014**, *29*, 1092–1099.
12. Zhou, Z.; Huang, J. Dynamic Scattering Approach for Solving the Radar Cross-Section of the Warship under Complex Motion Conditions. *Photonics* **2020**, *7*, 64. [[CrossRef](#)]
13. Ye, S.; Xiong, J. Dynamic RCS behavior of helicopter rotating blades. *Acta Aeronaut. Astronaut. Sin.* **2006**, *27*, 816–822.
14. Wong, S.K.; Riseborough, E.; Duff, G.; Chan, K.K. Radar cross-section measurements of a full-scale aircraft duct/engine structure. *IEEE Trans. Antennas Propag.* **2006**, *54*, 2436–2441. [[CrossRef](#)]
15. Jiang, Z.H. Research on Radar Target Characteristics of Unmanned Helicopter. *J. Astronaut. Metrol. Meas.* **2015**, *35*, 61–66.
16. Rajesh, N.; Malathi, K.; Raju, S.; Kumar, V.A.; Prasath, S.D.R.; Alsath, M.G.N. Design of Vivaldi antenna with wideband radar cross section reduction. *IEEE Trans. Antennas Propag.* **2017**, *65*, 2102–2105. [[CrossRef](#)]
17. Xiao, T.; Luo, D.; Zheng, X.; Ang, H.; Ji, A. Progress and challenges in unsteady aerodynamic optimization design of bionic flapping-wings. *Acta Aerodyn. Sin.* **2018**, *36*, 80–87.
18. Vasanelli, C.; Bögelsack, F.; Waldschmidt, C. Reducing the radar cross section of microstrip arrays using AMC structures for the vehicle integration of automotive radars. *IEEE Trans. Antennas Propag.* **2018**, *66*, 1456–1464. [[CrossRef](#)]
19. Yang, Y.; Lu, G. Simulation research on aerodynamic performance of counterbeat four-wing flapping wing aircraft. *Flight Dyn.* **2019**, *37*, 25–29.
20. Ozgun, O.; Kuzuoglu, M. A domain decomposition finite-element method for modeling electromagnetic scattering from rough sea surfaces with emphasis on near-forward scattering. *IEEE Trans. Antennas Propag.* **2018**, *67*, 335–345. [[CrossRef](#)]
21. Yang, Y.; Gu, X. Simulation Study on Aerodynamic Characteristics of Flapping-wing Aircraft with Multi-stage Wing and Multiple Degree of Freedom. *J. Syst. Simul.* **2019**, *31*, 2019.
22. Deck-Léger, Z.-L.; Zheng, X.; Caloz, C. Electromagnetic Wave Scattering from a Moving Medium with Stationary Interface across the Interluminal Regime. *Photonics* **2021**, *8*, 202. [[CrossRef](#)]
23. Guo, J.; Yin, H.C.; Ye, S.J.; Man, L.; Jia, Q. Novel technology for electromagnetic characteristic simulation of helicopter blades. *Acta Aeronaut. Et Astronaut. Sin.* **2019**, *40*, 322732.
24. Wang, C.; Li, Y.; Feng, M.; Wang, J.; Ma, H.; Zhang, J.; Qu, S. Frequency-selective structure with transmission and scattering deflection based on spoof surface plasmon polariton modes. *IEEE Trans. Antennas Propag.* **2019**, *67*, 6508–6514. [[CrossRef](#)]
25. Zhou, Z.; Huang, J. Study of RCS characteristics of tilt-rotor aircraft based on dynamic calculation approach. *Chin. J. Aeronaut.* **2022**, *35*, 426–437. [[CrossRef](#)]
26. Fu, Y.; Zhao, S. Design of the aircraft model for bionic dragonflies' flapping wings and analysis on the aerodynamic characteristics. *J. Mach. Des.* **2021**, *38*, 10, 79–87.
27. Wang, X.Y.; Dallmann, T.; Moch, R.; Heberling, D. ISAR tomography for full-polarimetric 3-D radar cross-section measurements. *IEEE Trans. Antennas Propag.* **2019**, *67*, 2853–2858. [[CrossRef](#)]
28. Zhou, Z.; Huang, J.; Wang, J. Compound helicopter multi-rotor dynamic radar cross section response analysis. *Aerosp. Sci. Technol.* **2020**, *105*, 106047. [[CrossRef](#)]
29. Peng, C.; Sun, L.; Wang, Y.; Tan, W.; Xiao, F. Control oriented longitudinal modeling and analysis of pigeon-like flapping-wing aircraft. *J. Beijing Univ. Aeronaut. Astronaut.* **2021**. [[CrossRef](#)]
30. Viet, H.; Lee, C.; Lee, J. Two-dimensional efficient broadband retrodirective metasurface. *IEEE Trans. Antennas Propag.* **2019**, *68*, 2451–2456.
31. Elbaz, A.; He, Z.; Gao, B.; Chi, J.; Su, E.; Zhang, D.; Liu, S.; Xu, H.; Liu, H.; Gu, Z. Design of a two-stage flapping wing bionic aircraft. *Electromechanical Eng. Technol.* **2021**, *50*, 9–12.
32. Zhou, Z.; Huang, J.; Chen, C.; Zhang, J. Keen Investigation of the Electromagnetic Scattering Characteristics of Tiltrotor Aircraft Based on Dynamic Calculation Method. *Photonics* **2021**, *8*, 175. [[CrossRef](#)]
33. Wang, Q.; Zhang, X.; Yan, X.; Wang, F.; Cheng, T. Design of a Surface Plasmon Resonance Temperature Sensor with Multi-Wavebands Based on Conjoined-Tubular Anti-Resonance Fiber. *Photonics* **2021**, *8*, 231. [[CrossRef](#)]